Dynamic PRC1-CBX8 stabilizes a porous structure of chromatin condensates

Michael Uckelmann[1], Vita Levina[1], Cyntia Taveneau[1,2], Xiao Han Ng[1], Varun Pandey[3], Qi Zhang[1], Sarena Flanigan[1], Minrui Li[1,4], Partha Pratim Das[3], Alex de Marco[1,2], Chen Davidovich[1,5,*]

[1] Department of Biochemistry and Molecular Biology, Biomedicine Discovery Institute, Faculty of Medicine, Nursing and Health Sciences, Monash University; Clayton, Victoria, 3800, Australia.

[2] ARC Centre of Excellence in Advanced Molecular Imaging, Monash University; Clayton, Victoria, 3800, Australia.

[3] Department of Anatomy and Developmental Biology, Development and Stem Cells Program, Monash Biomedicine Discovery Institute, Monash University; Clayton, Victoria, 3800, Australia.

[4] Faculty of Information Technology, Monash University; Clayton, Victoria, 3800, Australia.

[5] EMBL-Australia; Clayton, Victoria, 3800, Australia.

* Correspondence: Chen.Davidovich@monash.edu

Abstract

The compaction of chromatin is a prevalent paradigm in gene repression. Chromatin compaction is commonly thought to repress transcription by restricting chromatin accessibility. However, the spatial organisation and dynamics of chromatin compacted by gene-repressing factors are unknown. Using cryo-electron tomography, we solved the three-dimensional structure of chromatin condensed by the Polycomb Repressive Complex 1 (PRC1) in a complex with CBX8. PRC1-condensed chromatin is porous and stabilised through multivalent dynamic interactions of PRC1 with chromatin. Within condensates, PRC1 remains dynamic while maintaining a static chromatin structure. In differentiated mouse embryonic stem cells, CBX8-bound chromatin remains accessible. These findings challenge the idea of rigidly compacted polycomb domains and instead provides a mechanistic framework for dynamic and accessible PRC1-chromatin condensates.

Main

Chromatin structure is intricately linked to transcriptional activity[1]. Compacted or “closed” chromatin is generally associated with inhibition of transcription while “open”, more accessible chromatin is more prone to being transcribed[1]. Polycomb Repressive Complex 1 (PRC1) is a repressive chromatin modifier critical for organismal development[2,3]. PRC1 has been proposed to inhibit gene expression by tightly compacting chromatin in a process that often is considered to restrict chromatin accessibility[2–11]. However, direct evidence for

PRC1-compacted chromatin being inaccessible is sparse and mechanistic explanations remain unsatisfactory (reviewed in[11]). Furthermore, recent studies show that changes in chromatin accessibility are more gradual than the simple binary classification into “open” and “closed” chromatin suggests[12–15]. A challenge in consolidating these seemingly contradictory findings is limited information into how PRC1 influences the three dimensional structure of chromatin.

PRC1 complexes can include one of five different chromobox proteins (CBX), all homologous to the fly Polycomb (Pc)[16]. The CBX protein CBX2 forms condensates through liquid-liquid phase separation, providing a potential mechanism for the compartmentalization of facultative heterochromatin[9,10]. Phase separation is emerging as a mechanism for chromatin organisation through the association of self-similar domains[17]. Chromatin can form condensates in the presence of divalent cations and histone tails[17–20]. Within these condensates, chromatin has variably been described as liquid-like, formed through liquid-liquid phase separation[17,19], or as solid[20]. A recent structure of liquid-liquid phase-separated chromatin, condensed by magnesium cations without protein binding partners, revealed that nucleosomes organise into irregular assemblies[19]. The lack of apparent periodicity in chromatin geometry has also been noted in computational simulations and in first attempts to image chromatin in cells by cryo-electron tomography (cryo-ET)[21,22]. However, the structural arrangement of chromatin condensed by a repressive factor remained unknown.

Herein we describe the three dimensional cryo-ET structure of chromatin condensed by a polycomb-repressive complex. We focus on a PRC1 complex that includes CBX8 ($PRC1^{C8}$), a chromobox protein that is upregulated during cell differentiation[23] and has oncogenic potential[24,25]. We show that dynamic interactions between $PRC1^{C8}$ and chromatin promote condensates through polymer-polymer phase separation. Contrary to expectations, PRC1-condensed chromatin is not tightly compacted but stabilises a porous chromatin structure that allows largely unhindered diffusion of $PRC1^{C8}$.

Results

PRC1-chromatin condensates are porous and accessible

To determine the structure of polycomb-compacted chromatin and the mechanisms of polycomb-driven chromatin compaction, we reconstituted the system *in vitro*. The reconstitution included a chromatinized polycomb target gene (referred to as chromatin hereafter) and a purified recombinant PRC1 complex composed of RING1b, BMI1 and CBX8 ($PRC1^{C8}$) (Fig. 1a). The $PRC1^{C8}$ complex is pure (Fig. 1b), monodispersed (Fig. 1c) and retains H2A ubiquitylation activity comparable to the RING1b-BMI1 heterodimer (Fig. 1d).

When combined, chromatin and $PRC1^{C8}$ were sufficient to form spherical phase-separated condensates, apparent in phase-contrast and fluorescence imaging (Fig. 1e). Using two different fluorescence labels, we confirmed the presence of both chromatin and $PRC1^{C8}$

72 within the same condensates (Fig. 1e). Importantly, both PRC1^{C8} and chromatin are
73 necessary for chromatin condensation, while the individual components do not phase-
74 separate (Fig. 1e). PRC1^{C8}-chromatin condensates are preserved on an EM grid after
75 vitrification (Fig. 1f). This allowed us to study the internal molecular structure of PRC1^{C8}-
76 chromatin condensates by cryo-electron tomography (Fig. 1g). We collected tomograms
77 near the condensate border to observe the boundary conditions. The reconstruction allows
78 individual nucleosomes to be identified, revealing a dense network of hundreds of
79 nucleosomes with a distinct condensate boundary (Fig. 1G and Movie S1). We could not
80 unambiguously assign density to PRC1^{C8}, possibly because it adapts various conformations
81 while simultaneously using multiple surfaces to interact with chromatin (more below). The
82 final structure reflects the arrangement of nucleosomes in PRC1^{C8}-chromatin condensate
83 (Fig. 1g, second panel). Unexpectedly, the structure shows that PRC1^{C8} does not compact
84 nucleosomes into an impassable barrier. Instead, PRC1^{C8} rather stabilises chromatin in a
85 porous mesh-like structure (Fig. 1g). Analysing the orientation of individual nucleosomes
86 towards their neighbouring nucleosomes shows no obvious orientation bias (Extended Data
87 Fig. 1a,b). We conclude that PRC1^{C8} does not induce a substantial inter-nucleosome
88 orientation bias, but rather supports forming a porous chromatin structure.

89 We next wished to determine the size of macromolecules that could diffuse into PRC1-
90 chromatin condensates. We used the condensate structure to calculate solvent-excluded
91 volumes[26] with variable probe radii ranging from 0.2 nm to 20 nm (Fig. 1h,i). Interestingly,
92 the analysis shows that the condensate is accessible for macromolecules of a considerable
93 size of up to 8 nm in radius (equivalent to approximately 600 kDa). Small macromolecules
94 (<10 kDa), with radii below 2 nm, would have enough room to access every single
95 nucleosome. Conversely, access is increasingly restricted for molecules with a radius above
96 8 nm (approximately 600 kDa). This suggests that PRC1-chromatin condensates are
97 surprisingly accessible and that PRC1^{C8} itself would be able to move within these
98 condensates largely unhindered. To test this we next ventured to analyse PRC1 dynamics
99 within condensates experimentally.

100 **PRC1^{C8} is mobile and chromatin is static within PRC1-chromatin condensates**

101 Chromatin condensates form under close to physiological salt concentrations, at PRC1^{C8}
102 concentrations as low as 500 nM and are dependent on PRC1^{C8} (Fig. 2a) .We conclude that
103 PRC1^{C8} is sufficient to drive the formation of the chromatin condensates under
104 physiologically relevant conditions. We next asked if chromatin and PRC1 show different
105 dynamics within the condensates. Fluorescence recovery after photobleaching (FRAP) of
106 PRC1^{C8}-chromatin condensates shows fast recovery kinetics for GFP-labelled PRC1 (Fig. 2b,
107 in green). Conversely, we observed a very slow recovery for Cy5-labelled chromatin (Fig. 2b,
108 in red). We conclude that, within condensates, PRC1 is mobile while chromatin itself is static
109 (Fig. 2c). This confirms that PRC1^{C8} can diffuse largely unhindered within PRC1^{C8}-chromatin
110 condensates, in line with our structural analysis (Fig. 1h,i).

111 **Multivalent interactions between PRC1^{C8} and chromatin induce phase separation**

112 Previous studies have concluded that magnesium-driven chromatin condensates form *in*
113 *vitro* via liquid-liquid phase separation[17,19]. This view is challenged by the observation of
114 solid-like chromatin condensates in living cells[20]. Our observation that chromatin is static
115 within PRC1-chromatin condensates does not agree with liquid-like behaviour, but rather
116 suggests polymer-polymer phase separation (PPPS) as a mechanism for condensate
117 formation[27–29]. PPPS depends on one polymer acting as a scaffold that is condensed by the
118 second molecule binding to it via multivalent interactions, effectively acting like a
119 crosslinker[27–29].

120 To test for polymer-polymer phase separation of condensates, we next probed for
121 multivalent interactions between PRC1 and chromatin. The whole PRC1^{C8} complex (RING1b,
122 BMI1 and CBX8) is necessary and sufficient to condense chromatin, while the PRC1 core or
123 CBX8 alone do not condense chromatin (Fig. 3a). This suggests multivalent interactions
124 between the PRC1^{C8} complex and chromatin, involving different chromatin interacting
125 surfaces in both PRC1 and CBX8. To identify the different interaction sites, we first used
126 crosslinking mass spectrometry (XL-MS) to probe for protein-protein interactions within
127 PRC1^{C8}–chromatin condensates (Fig. 3b). The results show multiple crosslinks from the
128 CBX8 chromodomain to the H3 histone tail (Fig. 3b), indicative of binding. Interactions
129 between CBX-proteins and H3K27me3-modified H3-histone tails have been proposed to
130 recruit PRC1 to chromatin modified by PRC2[2,3]. However, CBX8 did crosslink to
131 unmethylated H3 tails (Fig. 3b) and a trimethyl-lysine analogue (MLA) at H3K27 did not
132 improve the chromatin-condensation activity of PRC1^{C8} (Fig. 3d). We conclude that
133 H3K27me3 is not necessary for the chromatin condensation activity of PRC1^{C8} and that the
134 H3 histone tail, even if unmodified, provides an interaction site for PRC1 on chromatin.

135 DNA has previously been shown to bind CBX8[30] and could provide another interaction site
136 for PRC1^{C8} on chromatin. We tested DNA binding in solution using a 24bp double stranded
137 DNA probe and found that CBX8 is necessary for the DNA-binding activity of PRC1^{C8} (Fig. 3c).
138 Hence, CBX8 binding to DNA provides a second interaction site of PRC1 with chromatin.

139 We conclude that PRC1 interacts with chromatin via at least three distinct sites: PRC1^{C8}
140 binds to DNA and the H3 tail via CBX8, as shown herein (Fig. 3), and binds the nucleosome
141 acidic patch via RING1b-BMI1 as shown elsewhere[31]. These multivalent interactions would
142 have to change dynamically while PRC1 maintains the condensed state of chromatin and
143 diffuses through it at the same time (Fig. 2b). Collectively, we propose that PRC1 induces
144 chromatin condensation via polymer-polymer phase separation, through dynamic
145 multivalent interactions between PRC1 and chromatin.

146 **CBX8 binding sites on chromatin in mouse embryonic stem cells are accessible**

147 Given the porous structure of PRC1^{C8}-condensed chromatin in vitro (Fig. 1) and the dynamic
148 diffusion of PRC1^{C8} within condensates (Fig. 2b), we next wished to probe for the
149 accessibility of PRC1^{C8}-bound chromatin in cells. We carried out the Assay for Transposase
150 Accessible Chromatin (ATAC-seq) in differentiated mESC, combined with ChIP-seq for CBX8
151 and H3K27me3. We used differentiated mESC, because CBX8 is expressed at very low levels
152 in pluripotent mESC and is upregulated during retinoic acid-induced cell differentiation ([23]
153 and Fig. 4a). The DNA-loaded Tn5 used in ATAC-seq experiments forms a dimeric complex of
154 approximately 130 kDa with an estimated hydrodynamic radius[32] of 4.6 nm (based on PDB
155 code 1MUH[33]). In agreement with the accessibility analysis *in vitro* (Fig. 1h), the majority of
156 CBX8 ChIP-seq peaks in cells overlapped with ATAC-seq peaks (Figure 4B), indicating they
157 are accessible to Tn5. This observation was persistent across the genome, where ATAC-seq
158 peaks are co-localised with CBX8 and H3K27me3 peaks (Fig. 4c), indicating that CBX8-target
159 genes are largely accessible. The insufficiency of CBX8 to restrict chromatin accessibility is
160 further supported by the similar ATAC-seq profiles of wildtype and *Cbx8* knockout mESCs
161 (Fig. 4c,f, compare blue to orange). Hence, although the overall chromatin accessibility is
162 reduced during mESC differentiation (Fig. 4d,e), in agreement with previous works,[34] this
163 process is not dependent on CBX8. Collectively, we show that CBX8-bound polycomb-
164 repressed chromatin is largely accessible in differentiated mECSs (Fig. 4b-f).

165 **Discussion**

166 In conclusion, we have shown that PRC1-CBX8 binds chromatin via multivalent interactions
167 and induces chromatin condensation through polymer-polymer phase separation. PRC1^{C8} is
168 dynamic within condensates while keeping chromatin in a static, solid-like state. We
169 established that PRC1^{C8} is sufficient to induce the solid condensed state of chromatin.

170 How can PRC1 condense chromatin but yet maintain a highly dynamic behaviour in the
171 nucleus? PRC1 is characterised with a short residence time on chromatin[35]. Solid-like
172 chromatin that is condensed by a mobile chromatin binder has been shown *in vitro* for a
173 truncation of the SAM-domain protein Polyhomeotic (Ph)[36] and in cells for HP1a at
174 chromocenters[20]. Yet, the mechanism allowing PRC1 and other gene-repressing factors to
175 condense chromatin while constantly diffusing in it remained largely unknown. Our cryo-EM
176 structure of PRC1-condensed chromatin explains how PRC1 can move in condensed
177 chromatin (Fig. 1), owing to the large pores that are formed between condensed
178 nucleosomes. The multivalent interactions between PRC1-CBX8 to chromatin provide PRC1
179 with multiple docking sites on chromatin: unmodified and modified H3 tail (Fig 3b-d), DNA
180 (Fig 3c) and the acidic patch of the nucleosome[31]. Hence, it is possible that PRC1-CBX8 can
181 constantly change its interactions with chromatin to maintain its condensed structure while
182 utilising its different chromatin-interacting surfaces to dynamically move around. Our data
183 indicate that chromatin condensation together with dynamic behaviour within chromatin
184 condensates is an intrinsic biophysical property of PRC1-CBX8. It is plausible that the
185 dynamic behaviour of PRC1 within chromatin condensates is required in order to allow PRC1

186 to modify nucleosomes by the H2AK119ub mark while holding them together. This
187 phenomenon might represent a broad paradigm of repressive chromatin.The internal
188 structure of PRC1-chromatin condensates is a porous network of nucleosomes (Fig. 1). Such
189 a structure could present a size-selective diffusion barrier, in agreement with its
190 permeability to PRC1 diffusion in vitro (Fig. 2) and Tn5 accessibility in cells (Fig. 4). Such a
191 size-selective diffusion barrier may contribute to gene repression by selectively excluding
192 transcriptional coactivators, which are commonly large protein complexes (>1MDa[12,37–39]).
193 This is in agreement with the inverse correlation between the density of chromatin domains
194 and the molecular weight of the chromatin modifiers present in them[12]. Transcription factor
195 size has also been suggested to determine access to different chromatin domains based on
196 simulations[40]. Combining our results with earlier findings[12,19,20,40], we propose that size-
197 selective exclusion may be part of a broader mechanism by which chromatin-interacting
198 proteins regulate the accessibility of repressive chromatin.

199 **Acknowledgements**: We would like to thank the Ramaciotti centre for electron microscopy
200 at Monash university for providing instrumentation, technical support and collecting cryo-ET
201 data, the Monash Proteomics facility for providing instrumentation and technical support
202 and the Monash Micro Imaging facility for providing instrumentation and technical support.
203 We would also like to acknowledge the MASSIVE HPC platform for providing high-
204 performance computing resources
205
206 **Funding:** This work was supported by an Australian research council (ARC) DECRA fellowship
207 DE210101669 (M.U.), Sylvia and Charles Viertel Senior Medical Research Fellowship (C.D.)
208 and the National Health and Medical Research Council (NHMRC) grant numbers
209 APP1162921, APP1184637 and APP2011767 (C.D.). C.D. is an EMBL-Australia Group Leader.
210
211 **Authors contributions:** C.D. and M.U. conceptualised the project and acquired funding,
212 M.U., V.L., C.T., X.H.N and M.L. carried out experiments and investigated, P.P.D. and V.P.
213 generated cell lines, S.F. and Q.Z. cloned and purified histone mutants, M.L. and M.U.
214 developed software, C.D., A.d.M. and P.P.D. supervised, M.U. and C.D. wrote the original
215 draft and all authors reviewed and edited the manuscript.
216
217 **Declaration of interests:** The authors declare no conflict of interest.
218
219 **Data and materials availability:** Next generation sequencing data (ATAC-seq and ChIP-seq)
220 are available under GEO accession number GSE220140. The map for tomogram #1 has been
221 deposited to the EMD (EMD-29022). All cryo-ET raw data has been deposited to EMPIAR
222 under accession number EMPIAR-11344. XL-MS data has been deposited to Pride
223 (PXD039589)
224

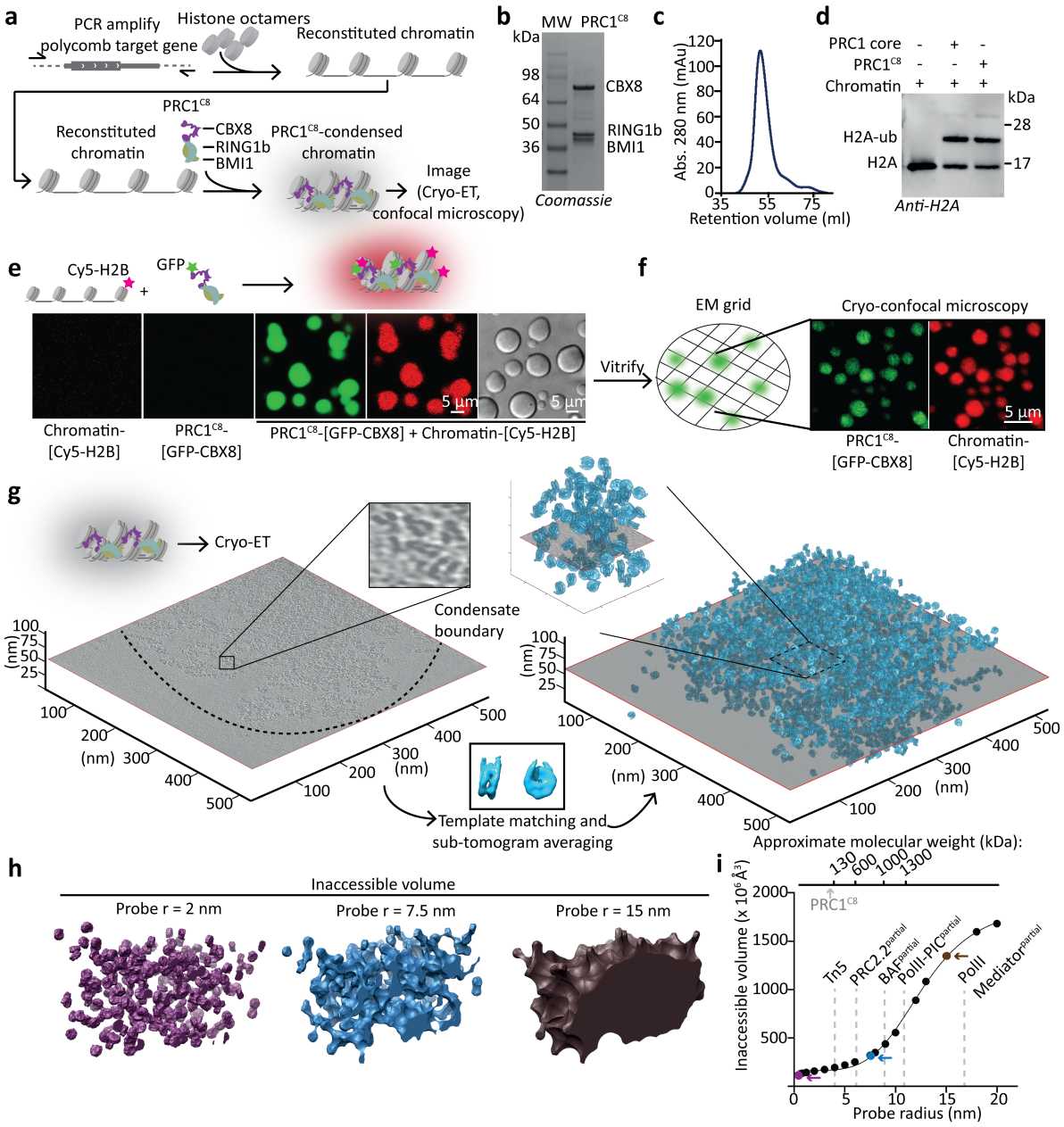

Fig. 1. The molecular structure of PRC1-chromatin condensates is porous and accessible to macromolecules. a, Schematics introducing the workflow. **b,** SDS-PAGE of purified PRC1^{C8} complex that includes RING1b, BMI1 and MBP-tagged CBX8. **c,** Size exclusion chromatography of the purified PRC1^{C8} using a HiLoad Sephacryl 300 16/60 column. **d,** In vitro ubiquitylation assay comparing PRC1^{C8} to a RING1b-BMI1 heterodimer. Samples in lane 2 and 3 included E1, E2, ubiquitin and ATP. Ubiquitylation is detected by western blot using an anti-H2A antibody. **e,** Chromatin condensates induced by the PRC1^{C8} complex and the individual proteins, visualised by confocal (left and centre) and phase contrast (right, from independent experiments) microscopy. CBX8 is GFP-labelled and chromatin is Cy5 labelled. Protein and chromatin concentrations are 1 µM and 20 nM, respectively. **f,** Cryo-confocal microscopy of vitrified PRC1^{C8}-chromatin condensates. **g,** Cryo-electron tomography of a PRC1^{C8}-chromatin condensate. Shown is a central slice through the

238 reconstruction (left image). Nucleosome subtomogram averages (centre, bottom) are then
239 placed in a volume the size of the tomographic slice, at the position and orientation
240 determined by template matching and subtomogram averaging (right image). **h,** Surface
241 representation of the volume of a subset of the PRC1^{C8}-chromatin condensate structure that
242 is inaccessible to probes of given radii. **i,** Inaccessible volumes for a given probe radii are
243 plotted, with exemplary molecules indicated (in grey) and selected probes coloured as in **h**.
244 For the indicated complexes, the hydrodynamic radius was estimated[32] using resolved
245 domains from published structures (see Methods section for PDB accessions) as a minimum
246 size estimate. See also Extended Data Figure 1.

247

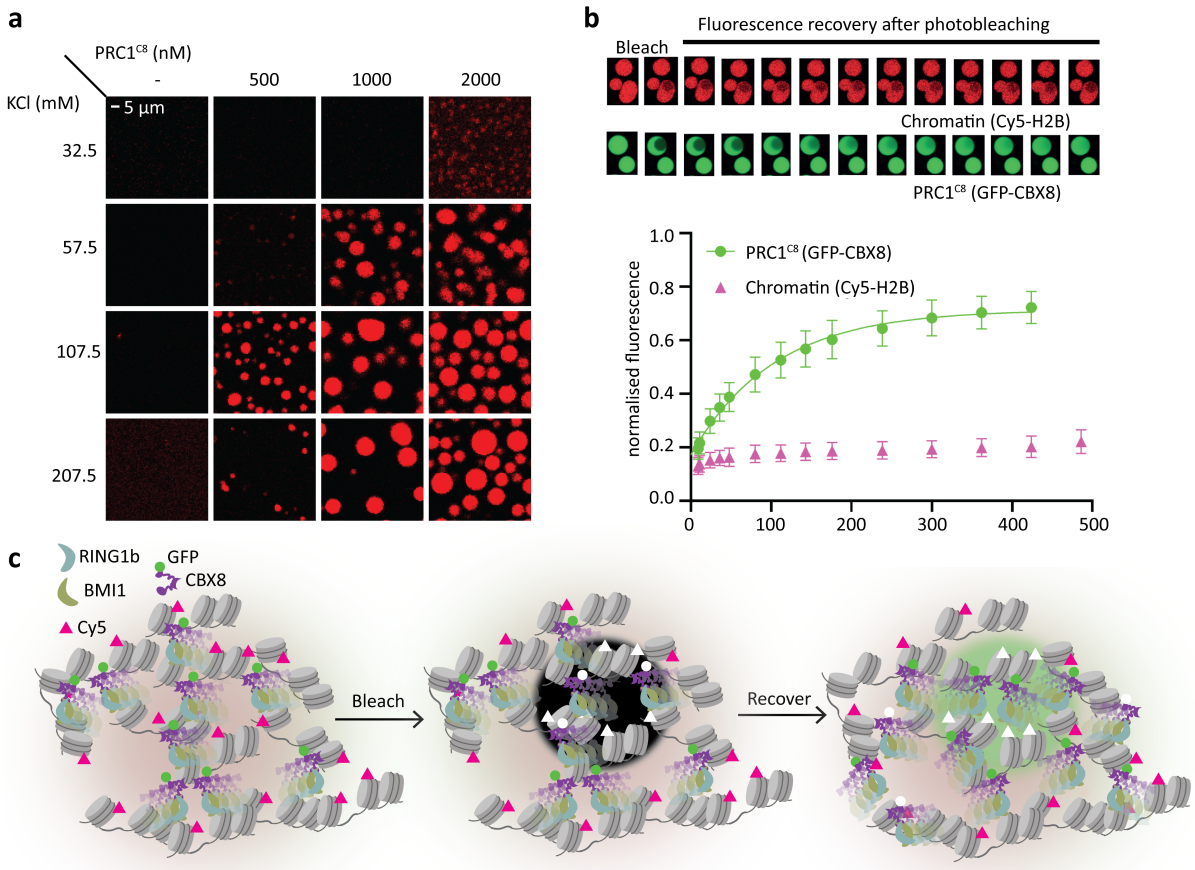

Fig. 2. PRC1^{C8} is mobile while chromatin is static within PRC1-chromatin condensates. **a,** Chromatin condensation in response to salt and PRC1 concentration measured by confocal microscopy using Cy5-labelled chromatin at a constant concentration of 50 ng/µl DNA. **b,** Representative micrographs of FRAP recorded in PRC1^{C8}-chromatin condensates. CBX8 is GFP labelled and chromatin is Cy5 labelled. Mean fluorescence intensity of the bleached area, normalised to pre-bleach mean signal, is plotted for every time point. Error bars show standard deviation from n=7 (GFP) and n=8 (Cy5) measurements recorded from two independent experiments. **c,** Schematic representation of the FRAP experiment.

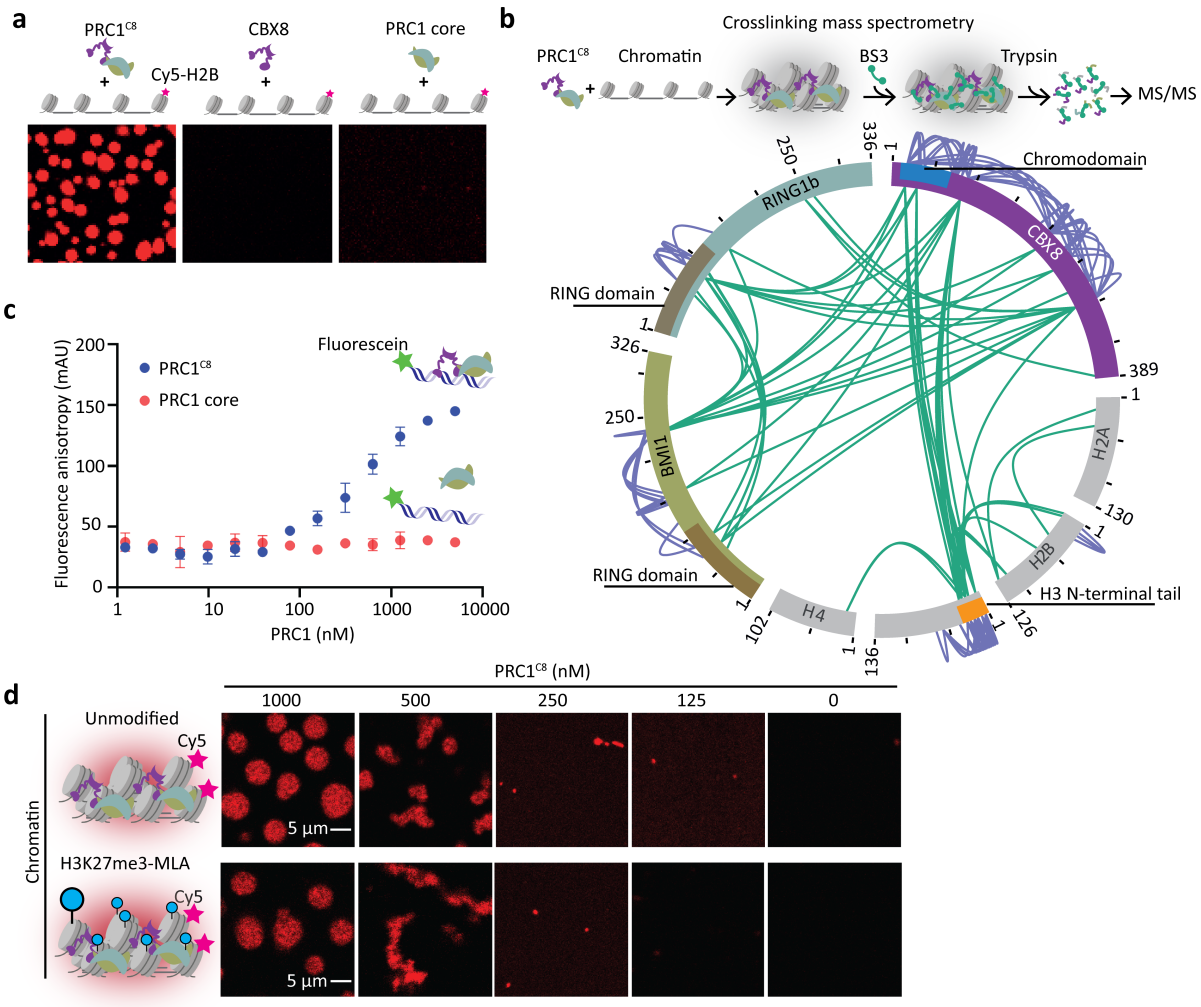

Fig. 3. Multivalent interactions between PRC1^{C8} and chromatin. a, Chromatin condensation in response to the whole PRC1^{C8} complex (RING1b, BMI1 and CBX8) or the individual components CBX8 and the RING1b–BMI1 heterodimer. Representative images from two replicates. **b,** Intermolecular (purple lines) and intramolecular (green lines) protein-protein interactions mapped within PRC1-chromatin condensates using crosslinking mass spectrometry (XL-MS). Data is from three independent replicates. **c,** PRC1^{C8} (blue) or PRC1 core (red) binding to a fluorescein labelled 24bp DNA probe measured by fluorescence anisotropy. Error bars show standard deviation based on two independent replicates. **d,** Titration of PRC1^{C8} to unmodified chromatin (top) and H3K27me3-MLA chromatin (bottom) at an identical chromatin concentration (50 ng/µl DNA) and 150 mM KCl. Micrographs are representative of two independent replicates.

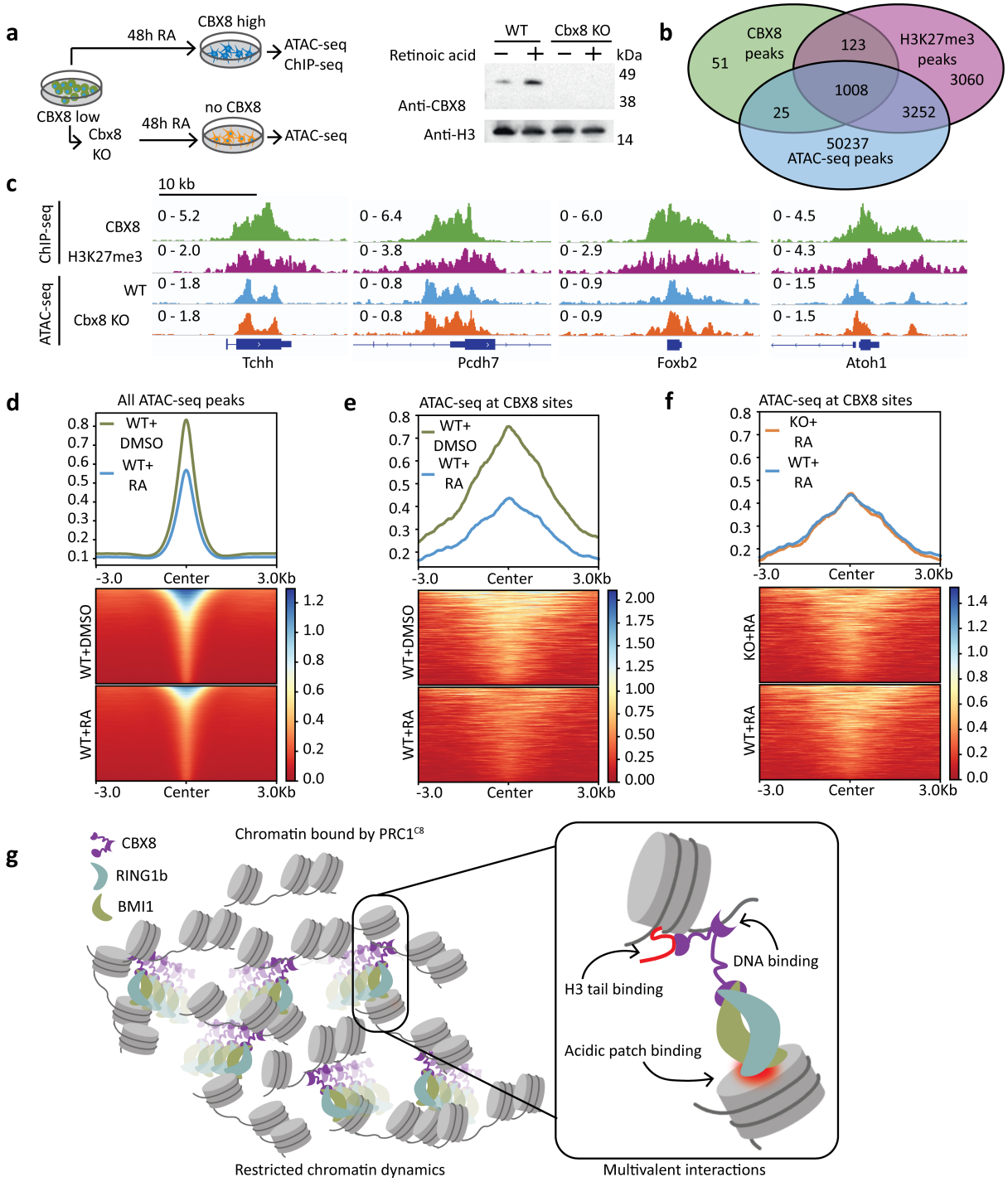

Fig. 4. CBX8 binding sites on chromatin in mouse embryonic stem cells are accessible. **a,** Schematics of the experimental setup (left) and anti-CBX8 western blot (right) of wildtype and *Cbx8* knockout mESC after 48 hours of retinoic acid (RA) treatment. **b,** Overlap of ATAC-seq peaks and CBX8 and H3K27me3 ChIP-seq peaks. ATAC-seq peaks are defined from two biological replicates. **c,** ChIP-seq traces for H3K27me3 and CBX8 in wildtype mESC and representative ATAC-seq traces at four genes in wildtype and CBX8 knockout mESC after 48 hours of RA treatment. **d,** Accessibility changes at all ATAC-seq peaks in wildtype (WT) mESC, in response to retinoic acid (RA) treatment. **e,** Accessibility changes at all CBX8-target sites in wildtype mESC, in response to RA treatment. **f,** Comparison of accessibility at CBX8-

280 target sites between wildtype and *Cbx8* knockout cells after RA treatment. **g,** Model: PRC1
281 forms multivalent interactions with chromatin, thereby stabilizing chromatin condensates.
282 These interactions dynamically change as PRC1 diffuses through condensates.
283

284 **Extended Data**

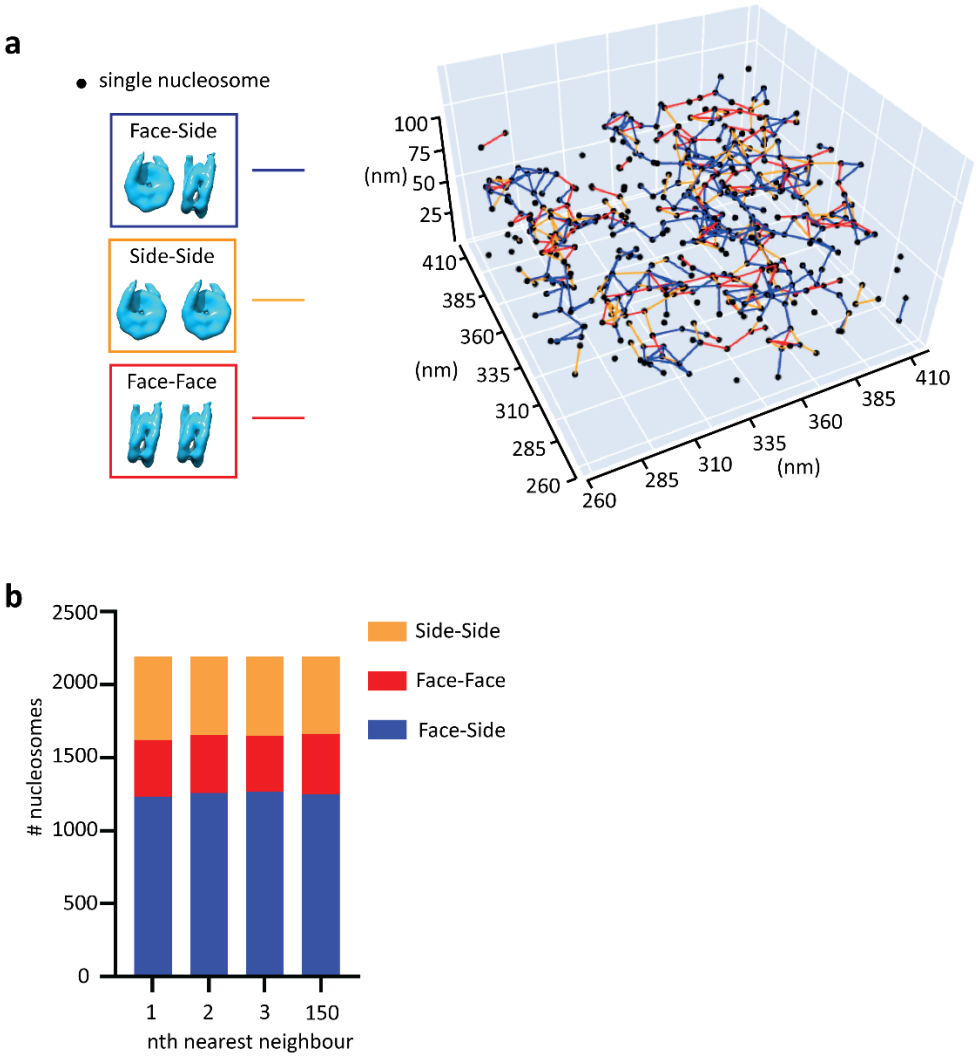

285
286 **Extended Data Fig. 1. Related to Fig. 1; Nucleosomes in PRC1^{C8}-chromatin condensates**
287 **show no orientation bias towards neighbouring nucleosomes. a,** Orientations of
288 nucleosomes towards neighbouring nucleosomes within a cut-off of 20 nm. Individual points
289 represent nucleosomes and lines between points are coloured according to the relative
290 orientation of neighbouring nucleosomes as indicated in the colour key (left). **b,** Distribution
291 of nucleosome-nucleosome orientation for the three nearest neighbours and the 150th
292 neighbour of each nucleosome in tomogram #1. Colours correspond to the same respective
293 orientations as in **a**.

294

295 **Extended Data Movie S1. Related to Fig.1; Cryo-tomogram of a PRC1^{C8}-chromatin**
296 **condensate.** The movie shows a scan through the z-axis of denoised[51] tomogram #1.
297

298 **Materials and Methods**

299 **Plasmids and cloning**

300

301 Human RING1b (Uniprot ID Q99496) and human BMI1 (Uniprot ID P35226) were cloned into
302 a pFBOH-mhl vector (Addgene plasmid # 62304) cleaved with BseRI using Gibson Assembly®
303 Master Mix (NEB #E2611L) using the primers indicated in Table S1.
304 Human CBX8 open reading frame (Uniprot ID Q9HC52-1 and NCBI Reference Sequence was
305 NM_020649.2) was obtained from gene synthesis (Gen9) cloned into a modified pFastBac1
306 pFB1.HMBP.A3.PrS.ybbR vector digested by XhoI and XmaI sites to include a N-terminal
307 6xHis-MBP tag. Cloning of the polycomb target gene ATOH1 into the pUC18 vector was
308 described previously[41]. Plasmids for expression of human histones (H2A, H2B, H3.1 and H4)
309 in *E.coli* were a kind gift from David Tremethick, Australian National University. UbcH5c WT
310 pET28a was a gift from Rachel Klevit (Addgene plasmid # 12643;
311 http://n2t.net/addgene:12643; RRID:Addgene_12643)[42].
312 pET3a-hUBA1 was a gift from Titia Sixma (Addgene plasmid # 63571;
313 http://n2t.net/addgene:63571; RRID:Addgene_63571)[43].
314 To generate a baculovirus expression vector of a monomeric EGFP-CBX8 (mEGFP-CBX8)
315 construct, first GFP was amplified from a pSpCas9(BB)-2A-GFP vector and CBX8 was
316 amplified from a pFB1.HMBP.A3.PrS.ybbR vector containing CBX8 as an insert.
317 Subsequently, EGFP-CBX8 was cloned into the pFBOH-mhl vector cleaved with BseRI via
318 Gibson assembly, with a Serine-Glycine-Serine linker between EGFP and CBX8. Finally, to
319 generate monomeric mEGFP-CBX8, alanine residue 207 in EGFP was mutated to Lysine using
320 a site directed mutagenesis kit (Takeda) and the mutagenesis primers listed in Table 1.

321

322 Table 1: Cloning and mutagenesis primers (5'-3')

mEGFP mutagenesis A207K fw	CTGAGCACCCAGTCCAAGCTGAG CAAAGACCC	Used for mutagenesis of CBX8-EGFP
mEGFP mutagenesis A207K rv	GGGGTCTTTGCTCAGCTTGGACT GGGTGCTCA	Used for mutagenesis of CBX8-EGFP
EGFP_fw_PFBOH_MHL	TTGTATTTCCAGGGCATGGTGAG CAAGGGCGAG	Used for Gibson assembly of mEGFP-CBX8 into pFBOH-mhl vector
EGFP rv with SGS linker	TGAAAGCTCACTTCCACTCTTGTA CAGCTCGTCCATGC	Used for Gibson assembly of mEGFP-CBX8 into pFBOH-mhl vector
CBX8 5' with SGS linker	TGTACAAGAGTGGAAGTGAGCTT TCAGCGGTGGGG	Used for Gibson assembly of mEGFP-CBX8 into pFBOH-mhl vector
CBX8 rv pFBOH_MHL	CAAGCTTCGTCATCATCATCTTTT	Used for Gibson assembly of

	CTCTTTAAAAAAGCCT	mEGFP-CBX8 into pFBOH-mhl vector
ATOH1 fw	GCAGAGCCCAAACATTCACACA	Used to amplify ATOH1 from pUC18 plasmid
ATOH1 rv	GCGGAGTTTCCTAAAAGACGCC	Used to amplify ATOH1 from pUC18 plasmid
H2BT120C fw	GTGACCTGCTATACCAGCAGCAAATAA	Used for mutagenesis of H2B
H2BT120C rv	GGTATAGCAGGTCACGGCTTTGGTGCC	Used for mutagenesis of H2B
RING1b pFBOH-mhl fw	ttgtatttccagggcTCTCAGGCTGTGCAGACAAAC	Used for Gibson assembly into pFBOH-mhl vector
RING1b pFBOH-mhl rv	caagcttcgtcatcaTTTGTGCTCCTTTGTAGGTGC	Used for Gibson assembly into pFBOH-mhl vector
BMI1 pFBOH-mhl fw	ttgtatttccagggcCATCGAACAACGAGAATCAAG	Used for Gibson assembly into pFBOH-mhl vector
BMI1 pFBOH-mhl rv	caagcttcgtcatcaACCAGAAGAAGTTGCTGATGA	Used for Gibson assembly into pFBOH-mhl vector
24bp DNA duplex Fluorescein labeled	GGCGCCCTGCCCCGCCTCGCTCTG	Fluorescein labeled DNA duplex used for binding assays. Only the top strand is shown. The dye was attached to the 3’ end of the top strand.

Protein expression and purification

PRC1^{C8}, PRC1 core and CBX8 were co-expressed in *Trichoplusia ni* insect cells using the Baculovirus system. CBX8 variably carried an N-terminal 6xHis-mEGFP or a N-terminal 6xHis-MBP tag. The purification protocols were identical regardless of the tag. Baculoviruses were generated as per manufacturers instructions (Thermo Fisher). The viral titre was determined using the MTT assay (Promega #G3580). *Trichoplusia ni* insect cells were infected at a density of 1.5 - 2 x 10^6 cells and incubated for 60 hours at 27 °C in a shaker.
The cells were spun down at 1500 relative centrifugal force (RCF). The pellet was resuspended in 100 ml of lysis buffer per litre of cell culture (20 mM HEPES-KOH pH 7.5, 400 mM NaCl, 25 mM Imidazol, 10 % Glycerol, 0.2 mM TCEP, 1 mM PMSF and EDTA-free Complete protease inhibitor (Thermo Fisher)). Lysis proceeded for 30-45 minutes at 4 °C while rotating. The lysate was then centrifuged at 29000 RCF for 20 minutes at 4 °C. The supernatant was transferred to a fresh tube and 5 ml of Ni-NTA resin (Qiagen) was added.

340 The samples were then incubated for 60 minutes at 4 °C while rotating and subsequently
341 centrifuged at 500 RCF for 5 minutes at 4 °C to settle the beads. About 90 % of the
342 supernatant was removed. The beads were resuspended in the remaining 10 % of
343 supernatant and transferred to 25 mm diameter gravity flow columns (Biorad). The beads
344 were allowed to settle before the remaining buffer was drained and the beads were then
345 washed with 12 CV of Buffer B (20 mM HEPES-KOH pH 7.5 at 20 °C, 500 mM NaCl, 25 mM
346 Imidazole, 10 % Glycerol, 0.2mM TCEP), followed by 30 CV of Buffer A (20 mM HEPES pH 7.5
347 at 20 °C, 100 mM NaCl, 25 mM Imidazole, 10 % Glycerol, 0.5 mM DTT or 0.2 mM TCEP). The
348 protein was then eluted in 6 CV Elution Buffer (20 mM HEPES-KOH pH 7.5 at 20 °C, 100 mM
349 NaCl, 400 mM Imidazole, 10 % Glycerol, 0.2 mM TCEP). The eluted protein was loaded onto
350 a Hitrap 5 ml Heparin column (Cytvia) equilibrated in IX Buffer A (20 mM HEPES pH 7.5 at
351 20 °C, 100 mM NaCl, 0.5 mM DDT or 0.2 mM TCEP) and the column was washed with 5 CV of
352 IX Buffer A. The proteins were resolved over a 20 CV gradient ranging from 0 % to 100 % IX
353 Buffer B (20 mM HEPES pH7.5 at 20 °C, 1000 mM NaCl, 0.5 mM DTT or 0.2mM TCEP). The
354 fractions were analysed on SDS-PAGE and fractions containing the protein complex of
355 interest with the expected subunits stoichiometry were pooled. The pooled fractions were
356 concentrated using a Amicon ultra 30K centrifugal filter (Merck, cat UFC903024) and
357 purified by size exclusion chromatography using a HiLoad Sephacryl 300 16/60 column
358 (Cytiva) equilibrated in GF Buffer (20 mM HEPES-KOH pH 7.5 at 20 °C, 150 mM NaCl, 0.5 mM
359 DTT). The collected fractions were analysed on SDS-PAGE and fractions containing the
360 protein complex of interest at the expected stoichiometry were pooled and concentrated to
361 a concentration of 1-2 mg/ml using an Amicon ultra 30K centrifugal filter (Merck, cat
362 UFC903024). The purified protein was then aliquoted and frozen in liquid nitrogen. The
363 purified proteins were stored at -80 °C until use.
364
365 Human UBA1, UBCH5C and Ubiquitin were purified as described previously[44]. Histone
366 proteins H2A, H2B, H2BT120C, H3 and H4 were purified as described previously[45], except
367 that the gel filtration step was omitted.
368
369
370 **Production and purification of DNA for chromatin reconstitution**
371
372 The ATOH1 polycomb target gene was amplified in a large scale 10 ml PCR reaction including
373 500 nM ATOH1 fwd and reverse primers (see Table 1), 4 µg of ATOH1-pUC18 template[41],
374 200 µM dNTP mix (Invitrogen), 3 % DMSO, 50 mM KCl, 10 mM Tris-HCl, pH 8.8, 1.5 mM
375 MgCl2, 0.01% sterile gelatin. The reaction mixture was divided into 96-well plates to include
376 50 µl per well and the following PCR program was run:
377
378

Temperature (°C)	Time	Number of

	(minutes)	Cycles
95	3:00	1
95	0:15	25
63	0:20	
72	8:00	
72	3:00	1

379
380
381 The PCR product was purified via ion exchange chromatography using a 5 ml HiTrap Q
382 column (GE Healthcare). The column was equilibrated in Buffer A (25 mM HEPES 7.5, 250
383 mM NaCl) and the sample was resolved using a linear gradient ranging from 0 % to 100 %
384 Buffer B (25 mM HEPES pH 7.5, 2 M NaCl). The fractions containing pure DNA were pooled,
385 subjected to ethanol-precipitation and resuspended in 10 mM Tris-HCl pH 7.5 at 20 °C, 0.1
386 mM EDTA.
387
388 **Chromatin reconstitution**
389
390 Histone Octamers were refolded as described previously[45]. All steps were done at 4 °C or on
391 ice. Chromatin was reconstituted following the salt-gradient dialysis protocol described
392 previously[45]. For large scale reconstitution, DNA and octamer were combined at an optimal
393 ratio that was determined at trial experiments for each batch of octamers and DNA. To
394 determine the optimal ratio of histone octamer to DNA, titration was carried out using
395 increasing amounts of octamer to a constant amount of DNA (molar ratios of 16:1, 18:1,
396 20:1, 22:1 of Octamer:DNA) following by salt gradient dialysis. For the salt gradient dialysis,
397 samples were initially dialysed in a buffer containing 10 mM Tris-HCl pH 7.5 at 20 °C, 2 M
398 KCl, 1 mM EDTA, 1 mM DTT. The initial buffer was then gradually exchanged for a low salt
399 buffer containing 10 mM Tris-HCl pH 7.5 at 20 °C, 250 mM KCl, 1 mM EDTA, 1 mM DTT over
400 the course of 18 hours, after which the salt exchange was complete. Samples were then
401 centrifuged at 21000 RCF for one minute, separated on a 1% agarose gel in TAE buffer and
402 stained with SYBR Safe (Sigma). The highest Octamer:DNA ratio at which chromatin
403 remained soluble after finishing salt dialysis was finally used for large scale reconstitution.
404 For large scale reconstitutions, the salt gradient dialysis was performed as above while
405 scaling up the reaction accordingly. Additionally, after conclusion of the salt gradient, the
406 samples were transferred to 400 ml of low salt buffer (10 mM TrisRIS-HCl pH 7.5 at 20 °C,
407 250 mM KCl, 1 mM EDTA, 1 mM DTT) and dialysed for another 2 hours. The samples were
408 finally dialysed against 1 litre of Chromatin Storage Buffer (10 mM TRIS-HCl pH 7.5, 10 mM
409 KCl) overnight.

410
411 **Reconstitution of Fluorescently labelled chromatin**
412
413 To allow site-specific labelling of histone H2B, a cysteine was introduced via site-directed
414 mutagenesis (H2BK120C, as previously described[46]) using mutagenesis primers indicated in
415 Table S1. H2BK120C was labelled with Cyanine5-maleimide (Lumiprobe cat #13080) as
416 described previously[46]. Labelled octamers were refolded as described above. Before
417 chromatin reconstitution, the unlabelled and labelled octamers were combined at a molar
418 ratio of 7:1 (unlabeled:labelled). Chromatin was then reconstituted as described above.
419
420 **Chromatin condensation assays**
421
422 Fluorescently labelled proteins and chromatin were protected from light whenever possible.
423 Chromatin condensation assays were done as described previously[17] with some
424 modifications. Assays were done in 384-well plates with #1.5 glass bottoms (MatTek
425 PBK384G-1.5-C). The wells were treated with 1 M NaOH for 1 hour at room temperature,
426 NaOH was removed and wells were washed with copious amounts of MilliQ water (MQ).
427 MQ was removed and 70 ul of 5k mPEG-silane (Sigma #JKA3037-1G, dissolved in 95% EtOH
428 to a final concentration of 25 mg/ml) was added to each well. The plates were sealed and
429 incubated overnight at room temperature. The mPEG-silane was removed, the wells were
430 washed once with 95 % EtOH, then rinsed with copious amounts of MQ and dried
431 completely in the fume hood.
432 The wells were then passivated by adding 40 ul of 20 mg/ml BSA (NEB) and incubated for at
433 least one hour at room temperature. The BSA was removed and the wells were washed
434 three times with Condensation Buffer (20 mM HEPES pH 7.5 at 20 °C, 0.2 mg/ml BSA, 10 %
435 Glycerol, 5 mM DTT and 150 mM KCl unless stated otherwise). The chromatin stock was
436 adjusted to a DNA concentration of 100 ng/ul and 150 mM KCl. The PRC1 complex was
437 diluted in Condensation buffer to a protein concentration equal to twice the final PRC1
438 assay concentration as stated. To induce condensation, 16 ul of the diluted PRC1 were
439 combined with 16 ul of the salt-adjusted chromatin dilution in PCR tubes. The samples were
440 incubated for 30 minutes at room temperature before being transferred to the 384-well
441 plate and incubated for a further 60 minutes at room temperature, so that the first images
442 were recorded 90 minutes after induction of condensation.
443 Images were recorded with a Nikon C1 scanning confocal microscope. GFP was excited with
444 a 488 nm laser, Cy5 was excited with a 561 nm laser. Linear contrast adjustments were
445 made with ImageJ. Where several micrographs are compared to each other, the same
446 contrast settings were used for all micrographs.
447 Phase contrast images were recorded with a Leica DMI8 imaging system.
448
449 **Chromatin ubiquitylation assay**
450

451 The salt concentration of the chromatin stock was adjusted to 100 mM KCl. The nucleosome
452 equivalent concentration of chromatin arrays was calculated by measuring the molar DNA
453 concentration and assuming that one DNA molecule is populated by 18 nucleosomes. The
454 reaction mixture included 750 nM of chromatin (nucleosome equivalent concentration), 500
455 nM $PRC1^{C8}$ or RING1b-BMI1 dimer, 100 nM hUBA1, 500 nM UBCH5C and 50 µM ubiquitin in
456 Ub-Buffer (25 mM HEPES-KOH pH 7.5 at 20 °C, 100 mM KCl, 3 mM MgCl and 2 mM DTT) and
457 started by adding ATP to a final concentration of 3 mM. 15 ul reactions were incubated at
458 30 °C for 45 minutes and the reaction was stopped by adding 5 ul of 4X NuPage LDS-loading
459 dye (Thermo Scientific cat #NP0008) supplemented with 5 % 2-mercaptoethanol. The
460 samples were separated on a 4-12% NuPage gel (Thermo Scientific cat #NP0321BOX) using
461 MES buffer (Thermo Scientific cat #NP0002) in the tank. The gels were then blotted onto a
462 nitrocellulose membrane (Amersham, cat #GE10600002) in Tris-Glycine transfer buffer +
463 20 % Ethanol (v/v) for 90 minutes in the cold room at 310 mAmp in a blotting tank (BioRad).
464 H2A was detected using anti-H2A primary antibodies (Merck Millipore Cat. # 07-146, 1:1000
465 titer) and HRP-conjugated secondary antibodies (Santa Cruz, cat #sc-2357, titler 1:5000).
466
467 **Sample preparation for cryo-electron tomography**
468
469 The $PRC1^{C8}$ complex was combined with chromatinized ATOH1 at a final concentration of
470 1.6 µM $PRC1^{C8}$ and 500 ng/ul DNA at a final salt concentration of 25 mM NaCl and 8.3 mM
471 KCl. Samples were incubated at room temperature for 30 minutes. Just before freezing, 5
472 nm gold nanoparticles were added at a 1:6 ratio (v/v). 3.5 ul of sample was applied to a
473 Quantifoil grid (R1.2/1.3 on 200 copper mesh, Quantifoil cat #N1-C14nCu20-01) and vitrified
474 in liquid ethane using the Vitrobot plunge freezer (Thermo Scientific) with the following
475 settings: Temperature 4°C, blot force -3, blot time 4 seconds, humidity 100%.
476
477 **Cryo-electron tomography data collection and processing**
478
479 The data was collected with a Titan Krios electron microscope (Thermo Fisher) at 300 keV
480 acceleration voltage using a Gatan K2 Summit camera (Gatan). A tilt series was acquired
481 ranging from -60 to 60 degrees with 3 degree increments and a nominal defocus of -2.5 µm.
482 A dose symmetric collection scheme was followed as described previously[47]. The pixel size
483 was 1.32 Angstrom, the total dose per tomogram was 144.32 e/A^2. Four frames were
484 collected per tilt (dose per frame 0.88 e/A^2).
485 The movies were motion corrected using motioncor2[48]. The motion corrected images were
486 combined into stacks and further processed with Imod[49] version 4.9.9. Imaging artefacts
487 were identified and removed with Imod's Ccderaser function. Tilts were aligned using the
488 gold fiducial markers and the final aligned stack was binned by a factor of 4. The defocus
489 was estimated using emClarity[50] and the estimated defocus was used in Imod for CTF
490 correction. The final tomogram was calculated using Imod's implementation of weighted
491 back projection. For visualisation, the tomogram was denoised using Topaz[51]. The denoised

492 tomogram was only used for visualisation (Figure 1 and Movie S1). The original non-
493 denoised tomograms were used for all further processing, including template matching and
494 subtomogram averaging.
495
496 **Template matching, subtomogram averaging and modelling the chromatin structure of**
497 **condensates from cryo-electron tomograms**

498 Two tomograms were selected for further processing (Tomogram #1 and Tomogram #2 in
499 the following). To avoid user bias, we used a template matching algorithm[52] with the
500 structure of a single nucleosome as template (EMD-8140[53]) to identify initial positions and
501 orientations for each nucleosome. The pixel size of the template was adjusted using
502 emClarity to match the unbinned pixel size of the tomogram[50]. The template was then
503 subjected to a low-pass filter of 30 Angstrom and binned by a factor of four to match the
504 binned tomogram. Template matching was done with the Matlab implementation of
505 Dynamo[52] using the "dynamo_match" function. The template was masked with a tight-
506 fitting mask with smooth edges. The scanning range was set to 360 degrees with 10 degree
507 steps. In-plane rotation was also scanned over 360 degrees with 10 degrees steps. Particles
508 that passed a cross-correlation cut-off of 0.17 (Tomogram #1) or 0.19 (Tomogram #2) were
509 selected for further analysis. Obvious false positives were removed manually.

510 The particles were cropped from the tomogram with a box size of 36 pixels. Nucleosome
511 position and orientation was refined over three rounds of subtomogram averaging[52]. As an
512 initial template for subtomogram averaging, we used an average from all cropped particles
513 after template matching, masked with a tight-fitting mask with smooth edges generated in
514 the Dynamo mask editor. Specific settings for the different rounds of subtomogram
515 averaging are detailed in Table 2. The resulting average structure of a nucleosome from the
516 subtomogram averaging was then used to populate a volume the size of the tomogram with
517 nucleosomes at the determined positions and orientations. The graphic depiction of the
518 final model (Figure 1G) was generated using the Dynamo Matlab implementation[52].
519
520 Table 2: Settings for subtomogram averaging in Dynamo

	Round 1	Round 2	Round 3
Iterations	3	3	3
References	1	1	1
Cone Aperture	100	16	8
Cone Sampling	5	2	1

Azymuth Rotation Range	100	16	8
Azymuth Rotation Sampling	5	2	1
Refine	0	0	4
Refine Factor	0	0	2
High Pass	2	2	2
Low Pass	7	8	8
Symmetry	c1	c1	c1
Particle Dimension	36	36	36
Shift Limits	5	4	2
Shift Limiting Ways	1	1	1
Seperation in Tomogram	0	0	0
Basic MRA	0	0	0
Threshold Parameter	0.5	0.6	0.6
Threshold Modus	2	2	2

Analysis of exclusion volume

Exclusion volumes for spherical molecules of various radii were calculated using 3V[26] as follows. First, the positional and rotational coordinates of the nucleosomes within Tomogram #1 were determined by template matching followed by subtomogram averaging, as described above. Next, the positional and rotational coordinates of the nucleosomes were tabulated from within a section of 300 pixels x 300 pixels x 150 pixels (corresponding to 158.4 nm x 158.4 nm x 87.0 nm at the x, y and z axes, respectively) centred on the pixel at location (650,650,80), which was large enough to include hundreds of nucleosomes but yet

532 sufficiently small to carry out the subsequent computational analysis. The dimensions of the
533 resulting table were converted to Angstrom by multiplying with a tomogram pixel size of
534 5.28 Angstrom/pixel. Next, the table including nucleosome positions was used by the
535 Dynamo function 'dtchimera' to generate a chimera cmd script that placed a pdb structure
536 of a single nucleosome (PDB 1KX4[54]) at the position and orientation defined for each
537 nucleosome in the table. At the end of this process, each of the nucleosomes within the
538 tomogram section is represented by the pdb coordinates of the nucleosome template. The
539 resulting model was saved as a pdb file and used as input for 3V[26]. Varying probe radii
540 ranging from 2 to 20 nm were used.
541
542 **Hydrodynamic radius calculation using protein structures**
543
544 The hydrodynamic radii of various proteins (Figure 1I) were calculated using the HullRad[32]
545 web server (http://52.14.70.9/). The PDB codes for the structures used are: 6LTJ (BAF[37]),
546 1MUH (Tn5[33]), 7O4J (PolII-PIC[39]), 6C24 (PRC2.2[55]), 8GXS (PolII-Mediator[56]). 6LTJ, 6C24, 8GXS
547 and 7O4J are only partial models as not all residues were assigned, therefore the calculated
548 hydrodynamic radius represents an estimate of the minimal complex size, while the actual
549 size of these complexes could be larger.
550
551 **Analysis of nucleosome-nucleosome orientation**
552
553 Nucleosome-nucleosome orientation was classified into face-face, face-side and side-side,
554 as described in[22]. The orientations were calculated from the output table of the template
555 matching and subtomogram averaging process in Dynamo[52] using the Matlab script
556 'calculate_orientation.m'. The nucleosome-nucleosome orientation plot (Fig. S1A) was
557 generated using the 'plot_edges' function from the python notebook
558 NCP_orientation_analysis.ipyn. Both scripts are available on Github
559 (https://github.com/MichaUckelmann/Chromatin-Structure-Analysis).
560
561 **Cryo-light microscopy**
562
563 The samples were prepared as described for cryo-electron tomography, without gold
564 nanoparticles and in a buffer containing 100 mM KCl. The vitrified grids were imaged using a
565 ZEISS LSM900 Airyscan2 with a Linkam CMS196V Cryo stage.
566
567 **Fluorescence recovery after photobleaching (FRAP)**
568
569 Samples and plates were prepared and images were recorded as described above for
570 chromatin condensation assays. 1 µM PRC1^{C8} with an N-terminal GFP tag was used. The
571 FRAP experiments were set up with the NIS-Elements software (Nikon). Regions of interest
572 (ROIs) were defined and a single image was recorded before bleaching. Then the ROI was

573 bleached using 488 nm (GFP) and 561 (Cy5) lasers. The bleaching time and laser power was
574 set so that approximately 80 % of fluorescence signal within the ROI was quenched.
575 Recovery was measured over 424 seconds, recording a total of 13 images.
576 The data was analysed with ImageJ, the mean pixel intensity of the bleached ROI was
577 quantified for each timepoint.
578
579 **DNA binding assays**
580
581 DNA binding was assayed using a 24 bp DNA (sequence see Table 1) with Fluorescein
582 attached to the top strand. The probe was protected from light wherever possible. The
583 probes were synthesised and delivered as duplexes (IDT). Probes were dissolved at a
584 concentration of 5 mM DNA in milliQ water. The probes were then diluted to 4 µM in
585 annealing buffer (20 mM HEPES-KOH, 150 mM NaCl) and heated to 95 °C for 5 minutes. The
586 probe was then left at room temperature for at least 1 hour to anneal before being diluted
587 to 20 nM in 20 mM HEPES-KOH pH 7.5 at 20 °C, 150 mM NaCl, 1 mg/ml BSA (NEB cat
588 #B9000S), 0.1% Tween20, 1 mM DTT. Serial protein dilutions of the PRC1^{C8} and RING1b-
589 BMI1 complexes were prepared in Protein Dilution Buffer (20 mM HEPES-KOH, 150 mM
590 NaCl, 1 mM DTT) ranging from 10000 nM to 2.44 nM. 20 ul of probe were mixed with 20 ul
591 of the respective protein dilution and transferred to a 384-well plate. The samples were
592 incubated for 30 minutes in the dark at room temperature and then read using a Pherastar
593 plate reader (BMG Labtech). The fluorescence anisotropy signal was normalised and the
594 curves were fitted with a specific binding model with Hill slope (GraphPad Prism).
595
596 **Crosslinking mass spectrometry (XL-MS)**
597
598 Reconstituted chromatin was dialysed overnight against 1 litre of XL buffer (25 mM HEPES-
599 KOH pH 7.5 at 20 °C, 150 mM NaCl, 1 mM DTT). The chromatin was combined with PRC1^{C8} in
600 a 1:1.5 molar ratio (Nucleosomes:PRC1^{C8}). Specifically, the nucleosome equivalent
601 concentration of the chromatin array was calculated from the measured DNA concentration
602 assuming 18 nucleosomes per DNA molecule. 1.5 µM PRC1 and 1 µM nucleosome
603 equivalent concentration of chromatin arrays were then combined in XL buffer and
604 incubated for 30 minutes at room temperature. Crosslinking was done as described
605 before[57]. The bis(sulfosuccinimidyl)suberate (BS3) crosslinker was added to a final
606 concentration of 500 µM and crosslinking proceeded for 20 minutes at room temperature at
607 a reaction volume of 15 µl. The reaction was stopped by the addition of Tris-HCl pH 8 at
608 20 °C to a final concentration of 125 mM. The samples were then diluted to a volume of
609 100 µL using a buffer containing 50 mM Tris pH 8 at 20 °C and 150 mM NaCl. TCEP was
610 added to a final concentration of 10 mM and the samples were incubated at 60 °C for
611 30 min. Chloroacetamide was added to a final concentration of 40 mM and the samples
612 were incubated in the dark for 20 min. The samples were then digested using trypsin
613 (Promega cat #V5280) at 37 °C overnight. The digest was stopped by adding formic acid to a

614 final concentration of 1% v/v. The digested samples were purified using 100 µl ZipTip pipette
615 tips (Merck cat #ZTC18S960) according to the manufacturer's instructions. Samples were
616 then concentrated to ~5 µL using a SpeedVac vacuum centrifuge and diluted with 20 µL
617 Buffer A (0.1% v/v formic acid).
618
619 The peptides were analyzed by online nano-high-pressure liquid chromatography (UHPLC)
620 electrospray ionization-tandem mass spectrometry (MS/MS) on an Q Exactive Plus
621 Instrument connected to an Ultimate 3000 UHPLC (Thermo-Fisher Scientific). Peptides
622 reconstituted in 0.1% formic acid were loaded onto a trap column (Acclaim C18 PepMap 100
623 nano Trap, 2 cm × 100 µm I.D., 5-µm particle size and 300-Å pore size; Thermo-Fisher
624 Scientific) at 15 µL/min for 3 min before switching the precolumn in line with the analytical
625 column (Acclaim C18 PepMap RSLC nanocolumn, 75 µm ID × 50 cm, 3-µm particle size, 100-
626 Å pore size; Thermo-Fisher Scientific). The separation of peptides was performed at
627 250 nL/min using a non-linear acetonitrile (ACN) gradient of buffer A (0.1% formic acid) and
628 buffer B (0.1% formic acid, 80% ACN), starting at 2.5% buffer B to 42.5% over 95 min. Data
629 were collected in positive mode using a Data Dependent Acquisition m/z of 375–2000 as the
630 scan range, and higher-energy collisional dissociation (HCD) for MS/MS of the 12 most
631 intense ions with z 2–5. Other instrument parameters were: MS1 scan at 70,000 resolution,
632 MS maximum injection time 118 ms, AGC target 3E6, ion intensity threshold of 4.2e4 and
633 dynamic exclusion set to 15 s. MS/MS resolution of 35000 at Orbitrap with the maximum
634 injection time of 118 ms, AGC of 5e5 and HCD with collision energy = 27%.
635 For the data analysis, Thermo raw files were analysed using the pLink 2.3.4 search engine[58]
636 to identify crosslinked peptides, searching against the sequences of RING1b, BMI1, CBX8,
637 H2A, H2B, H3 and H4. The default settings for searches were used. N-terminal acetylation
638 and methionine oxidation were used as variable modifications and carbamidomethyl on
639 cysteines as a fixed modification. False discovery rates of 1% for peptide spectrum match
640 level were applied by searching a reverse database. Crosslinked peptides were further
641 analysed using the crissrosslinkeR package[59]. Specifically, peptides were retained by
642 crissrosslinkeR only if they passed a p-value cutoff of 0.05 or were present in at least two of
643 three replicates. Subsequent visualisation of retained peptide was carried out with xiNET[60].
644
645 **Generation of Cbx8 KO mESC lines using CRISPR/Cas9**
646
647 Paired sgRNAs were designed to delete exons 1–4 of the murine *Cbx8* gene. The Golden
648 Gate Cloning method was used to clone the sgRNAs (sequence below) into the lentiguide-
649 mCherry-Cas9 plasmid[61,62]. 2 million mESCs were transfected with 1 µg of each plasmid
650 carrying sgRNAs-mCherry-Cas9, using electroporation (Neon™ Transfection System
651 MPK5000). The following day, mCherry-positive mESCs were sorted by FACS and plated on a
652 10 cm dish at a very low density for single-cell clone picking. After 5-6 days, individual
653 colonies (derived from single cells) were picked, expanded, and genotyped using genomic
654 PCR to identify homozygous/biallelic deletions of Cbx8 KO mESC colonies. Selected Cbx8 KO

655 mESC lines were further confirmed by western blot for CBX8 (Cell Signalling, CBX8 (D2O8C),
656 cat # 14696S, titer 1:50 (Fig. 4a)) and HRP-conjugated secondary antibodies (Santa Cruz, cat
657 #sc-2357, titer 1:10000).
658
659 **Cbx8 sgRNA sequences (5' and 3' sgRNAs)**
660 CBX8-5'Fw: CACCTGCGAATGCGCCGCTTCAGG
661 CBX8-5'Rv: AAACCCTGAAGCGGCGCATTCGCA
662 CBX8-3'Fw: CACCCTCTATGGCCCCAAAAAGCG
663 CBX8-3'Rv: AAACCGCTTTTTGGGGCCATAGAG
664 **Cbx8 genotyping primers:**
665 Deletion_Fw: GCCTTCTGGTGCAGCTAAGT
666 Deletion_Rv: GACGTCAGCGGGAGAGTATT
667 Internal_Fw: CACCAAATGAATGCTCCAAA
668 Internal_Rv (same as the Deletion_Rv): GACGTCAGCGGGAGAGTATT
669
670 **Mouse embryonic stem cell culture**
671
672 Wildtype and *Cbx8* knockout mES cells were grown on gelatinized culture dishes in DMEM,
673 20 % FBS, 1x non-essential amino acids (Gibco #11140-050), 1x Glutamax (Gibco #35050-
674 061), PenStrep 100 u/ml (Thermo Fischer), 0.5 x EmbryoMax 2-Mercaptoethanol (Merck
675 Millipore #ES-007-E), 2.5 µg/ml Plasmocin (Invivogen), 1000 U/ml ESGRO Leukemia
676 Inhibitory Factor (LIF) (Merck Millipore cat #ESG1107).
677
678 **Mouse embryonic stem cell differentiation ahead of ChIP-seq and ATAC-seq**
679
680 Differentiation was induced by seeding cells at a density of $0.3x10^6$ cells per well in 6-well
681 plates (for ATAC-seq) or at $1.5x10^6$ cells per 10-cm culture dish (for ChIP-seq) in media
682 containing 1 µM all-trans retinoic acid (RA,Sigma-Aldrich R2625-50MG) and no LIF. Cells
683 were differentiated for 48 hours and the media was changed after 24 hours. Control cells
684 were treated with a DMSO volume equivalent to the RA volume in the differentiating cells.
685 After 48 hours, the cells were harvested, washed once with PBS, counted and used
686 immediately in either ChIP-seq or ATAC-seq experiments.
687
688 **ChIP-seq**
689
690 ChIP-seq was done as described previously[63]. 1.5 µg of CBX8 antibody (Cell Signalling, CBX8
691 (D2O8C), cat # 14696S) and 3 µg of H3K27me3 antibody (Tri-Methyl-Histone H3 (Lys27)
692 (C36B11), cat #35861SF) were used. Libraries were prepared using NEBNext ultra II DNA
693 library kit for Illumina (NEB Biolabs) according to the manufacturer instructions. The

resulting libraries were assessed for quality on a High Sensitivity D1000 Screen Tape (Agilent) and were sequenced using an Illumina Novaseq 6000 sequencer (Genewiz/Azenta).

Data processing for Chip-seq

The reads were quality-trimmed and adapters were removed using Trim Galore!, a wrapper script to cutadapt[64], in paired end mode and using default settings. The reads were then aligned to the mouse mm10 genome build using bowtie2[65] with the option "very-sensitive". The data was reduced to only properly paired reads using "samtools view" with the flag "-f 3". PCR duplicates were removed using the RemoveDuplicates function from Picard Tools. Read mates were fixed using samtools fixmate. BigWig files were calculated using BamCoverage with CPM normalisation.
Peaks were called with Macs2[66] callpeak function, using the input sample as control. For the CBX8 ChIP-seq data set, default settings with a q-value cut-off of 0.05 were used. For H3K27me3 ChIP-seq data set, broad mode was used with a q-value and broad cutoff of 0.001. Peaks overlapping with ENCODE blacklisted regions[67] were removed.

ATAC-seq

ATAC-seq was done using a commercial kit (Diagenode Cat.# C01080002) according to the instructions of the manufacturer. The resulting libraries were assessed for quality control on a High Sensitivity D1000 Screen Tape (Agilent) and libraries were sequenced using an Illumina Novaseq 6000 sequencer (Genewiz/Azenta).

Data processing ATAC-seq

ATAC-seq data was processed as described previously[68]. Specifically, reads were quality-trimmed and adapters were removed using Trim Galore!, a wrapper script to cutadapt[64], in paired end mode using default settings. The reads were then aligned to the mouse mm10 genome build using bowtie2[65] with the option "very-sensitive". Reads were sorted and indexed using Samtools. Mitochondrial reads were removed using a python script from Harvard Bioinformatics (available at https://github.com/harvardinformatics/ATAC-seq). The data was reduced to only properly paired reads using "samtools view" with the flag "-f 3". The library complexity was estimated and the data sets were subsampled to reach a similar complexity as described previously[68]. PCR duplicates were removed using the RemoveDuplicates function from Picard Tools. Read mates were fixed using samtools fixmate. BigWig files were calculated using BamCoverage with CPM normalisation
For peak calling the bam files were converted to BEDPE files and the Tn5 shift was corrected by running a bash script provided at https://github.com/reskejak/ATAC-seq (bedpeTn5Shift.sh). Files were then converted to minimal bed format and peaks were called using Macs2[66] callpeak function in broad mode with broad-cutoff set to 0.05. Peaks

735 overlapping with ENCODE blacklisted regions[67] were removed. Consensus peaks for each
736 condition were defined as the intersect of peaks from both biological replicates. Venn
737 diagrams were generated using the ChIPPeakAnno package[69].
738
739
740
741
742
743

744 **References**

745 1. Misteli, T. The Self-Organizing Genome: Principles of Genome Architecture and
746 Function. *Cell* **183**, 28–45 (2020).
747 2. Schuettengruber, B., Bourbon, H.-M., Di Croce, L. & Cavalli, G. Genome Regulation by
748 Polycomb and Trithorax: 70 Years and Counting. *Cell* **171**, 34–57 (2017).
749 3. Blackledge, N. P., Rose, N. R. & Klose, R. J. Targeting Polycomb systems to regulate
750 gene expression: modifications to a complex story. *Nat Rev Mol Cell Biol* **16**, 643–649
751 (2015).
752 4. Eskeland, R. *et al.* Ring1B Compacts Chromatin Structure and Represses Gene
753 Expression Independent of Histone Ubiquitination. *Molecular Cell* **38**, 452–464 (2010).
754 5. Francis, N. J., Kingston, R. E. & Woodcock, C. L. Chromatin Compaction by a Polycomb
755 Group Protein Complex. *Science* **306**, 1574–1577 (2004).
756 6. Grau, D. J. *et al.* Compaction of chromatin by diverse Polycomb group proteins requires
757 localized regions of high charge. *Genes Dev.* **25**, 2210–2221 (2011).
758 7. Lau, M. S. *et al.* Mutation of a nucleosome compaction region disrupts Polycomb-
759 mediated axial patterning. *Science* **355**, 1081–1084 (2017).
760 8. Isono, K. *et al.* SAM Domain Polymerization Links Subnuclear Clustering of PRC1 to
761 Gene Silencing. *Developmental Cell* **26**, 565–577 (2013).
762 9. Tatavosian, R. *et al.* Nuclear condensates of the Polycomb protein chromobox 2 (CBX2)
763 assemble through phase separation. *Journal of Biological Chemistry* **294**, 1451–1463
764 (2019).
765 10. Plys, A. J. *et al.* Phase separation of Polycomb-repressive complex 1 is governed by a
766 charged disordered region of CBX2. *Genes Dev.* **33**, 799–813 (2019).
767 11. Illingworth, R. S. Chromatin folding and nuclear architecture: PRC1 function in 3D.
768 *Current Opinion in Genetics & Development* **55**, 82–90 (2019).
769 12. Miron, E. *et al.* Chromatin arranges in chains of mesoscale domains with nanoscale
770 functional topography independent of cohesin. *Science Advances* **6**, eaba8811 (2020).

771 13. Nozaki, T. *et al.* Dynamic Organization of Chromatin Domains Revealed by Super-
772 Resolution Live-Cell Imaging. *Molecular Cell* **67**, 282-293.e7 (2017).
773 14. Murphy, S. & Boettiger, A. N. Polycomb repression of Hox genes involves spatial
774 feedback but not domain compaction or demixing. 2022.10.14.512199 Preprint at
775 https://doi.org/10.1101/2022.10.14.512199 (2022).
776 15. King, H. W., Fursova, N. A., Blackledge, N. P. & Klose, R. J. Polycomb repressive
777 complex 1 shapes the nucleosome landscape but not accessibility at target genes.
778 *Genome Res.* **28**, 1494–1507 (2018).
779 16. Chittock, E. C., Latwiel, S., Miller, T. C. R. & Müller, C. W. Molecular architecture of
780 polycomb repressive complexes. *Biochemical Society Transactions* **45**, 193–205 (2017).
781 17. Gibson, B. A. *et al.* Organization of Chromatin by Intrinsic and Regulated Phase
782 Separation. *Cell* **179**, 470-484.e21 (2019).
783 18. Maeshima, K. *et al.* Nucleosomal arrays self-assemble into supramolecular globular
784 structures lacking 30-nm fibers. *The EMBO Journal* **35**, 1115–1132 (2016).
785 19. Zhang, M. *et al.* Molecular organization of the early stages of nucleosome phase
786 separation visualized by cryo-electron tomography. *Molecular Cell* **82**, 3000-3014.e9
787 (2022).
788 20. Strickfaden, H. *et al.* Condensed Chromatin Behaves like a Solid on the Mesoscale In
789 Vitro and in Living Cells. *Cell* **183**, 1772-1784.e13 (2020).
790 21. Cai, S., Böck, D., Pilhofer, M. & Gan, L. The in situ structures of mono-, di-, and
791 trinucleosomes in human heterochromatin. *MBoC* **29**, 2450–2457 (2018).
792 22. Farr, S. E., Woods, E. J., Joseph, J. A., Garaizar, A. & Collepardo-Guevara, R.
793 Nucleosome plasticity is a critical element of chromatin liquid–liquid phase separation
794 and multivalent nucleosome interactions. *Nat Commun* **12**, 2883 (2021).
795 23. Morey, L. *et al.* Nonoverlapping Functions of the Polycomb Group Cbx Family of
796 Proteins in Embryonic Stem Cells. *Cell Stem Cell* **10**, 47–62 (2012).
797 24. Chung, C.-Y. *et al.* Cbx8 Acts Non-canonically with Wdr5 to Promote Mammary
798 Tumorigenesis. *Cell Reports* **16**, 472–486 (2016).

799 25. Tan, J. *et al.* CBX8, a Polycomb Group Protein, Is Essential for MLL-AF9-Induced
800 Leukemogenesis. *Cancer Cell* **20**, 563–575 (2011).
801 26. Voss, N. R. & Gerstein, M. 3V: cavity, channel and cleft volume calculator and extractor.
802 *Nucleic Acids Research* **38**, W555–W562 (2010).
803 27. Barbieri, M. *et al.* Complexity of chromatin folding is captured by the strings and binders
804 switch model. *Proceedings of the National Academy of Sciences* **109**, 16173–16178
805 (2012).
806 28. Erdel, F. & Rippe, K. Formation of Chromatin Subcompartments by Phase Separation.
807 *Biophysical Journal* **114**, 2262–2270 (2018).
808 29. Lawrimore, J. *et al.* The rDNA is biomolecular condensate formed by polymer–polymer
809 phase separation and is sequestered in the nucleolus by transcription and R-loops.
810 *Nucleic Acids Research* **49**, 4586–4598 (2021).
811 30. Connelly, K. E. *et al.* Engagement of DNA and H3K27me3 by the CBX8 chromodomain
812 drives chromatin association. *Nucleic Acids Research* **47**, 2289–2305 (2019).
813 31. McGinty, R. K., Henrici, R. C. & Tan, S. Crystal structure of the PRC1 ubiquitylation
814 module bound to the nucleosome. *Nature* **514**, 591–596 (2014).
815 32. Fleming, P. J. & Fleming, K. G. HullRad: Fast Calculations of Folded and Disordered
816 Protein and Nucleic Acid Hydrodynamic Properties. *Biophysical Journal* **114**, 856–869
817 (2018).
818 33. Davies, D. R., Goryshin, I. Y., Reznikoff, W. S. & Rayment, I. Three-Dimensional
819 Structure of the Tn5 Synaptic Complex Transposition Intermediate. *Science* **289**, 77–85
820 (2000).
821 34. Meléndez-Ramírez, C. *et al.* Dynamic landscape of chromatin accessibility and
822 transcriptomic changes during differentiation of human embryonic stem cells into
823 dopaminergic neurons. *Sci Rep* **11**, 16977 (2021).
824 35. Huseyin, M. K. & Klose, R. J. Live-cell single particle tracking of PRC1 reveals a highly
825 dynamic system with low target site occupancy. *Nat Commun* **12**, 887 (2021).

826 36. Seif, E. *et al.* Phase separation by the polyhomeotic sterile alpha motif
827 compartmentalizes Polycomb Group proteins and enhances their activity. *Nat Commun*
828 **11**, 5609 (2020).
829 37. He, S. *et al.* Structure of nucleosome-bound human BAF complex. *Science* **367**, 875–
830 881 (2020).
831 38. Wang, H. *et al.* Structure of the transcription coactivator SAGA. *Nature* **577**, 717–720
832 (2020).
833 39. Schilbach, S., Aibara, S., Dienemann, C., Grabbe, F. & Cramer, P. Structure of RNA
834 polymerase II pre-initiation complex at 2.9 Å defines initial DNA opening. *Cell* **184**, 4064-
835 4072.e28 (2021).
836 40. Maeshima, K. *et al.* The physical size of transcription factors is key to transcriptional
837 regulation in chromatin domains. *J. Phys.: Condens. Matter* **27**, 064116 (2015).
838 41. Zhang, Q. *et al.* PALI1 facilitates DNA and nucleosome binding by PRC2 and triggers an
839 allosteric activation of catalysis. *Nat Commun* **12**, 4592 (2021).
840 42. Brzovic, P. S., Lissounov, A., Christensen, D. E., Hoyt, D. W. & Klevit, R. E. A
841 UbcH5/Ubiquitin Noncovalent Complex Is Required for Processive BRCA1-Directed
842 Ubiquitination. *Molecular Cell* **21**, 873–880 (2006).
843 43. Pichler, A. *et al.* SUMO modification of the ubiquitin-conjugating enzyme E2-25K. *Nat*
844 *Struct Mol Biol* **12**, 264–269 (2005).
845 44. Uckelmann, M. *et al.* USP48 restrains resection by site-specific cleavage of the BRCA1
846 ubiquitin mark from H2A. *Nat Commun* **9**, 229 (2018).
847 45. Luger, K., Rechsteiner, T. J. & Richmond, T. J. Preparation of nucleosome core particle
848 from recombinant histones. in *Methods in Enzymology* vol. 304 3–19 (Academic Press,
849 1999).
850 46. Sabantsev, A., Levendosky, R. F., Zhuang, X., Bowman, G. D. & Deindl, S. Direct
851 observation of coordinated DNA movements on the nucleosome during chromatin
852 remodelling. *Nat Commun* **10**, 1720 (2019).

853 47. Hagen, W. J. H., Wan, W. & Briggs, J. A. G. Implementation of a cryo-electron
854 tomography tilt-scheme optimized for high resolution subtomogram averaging. *Journal of*
855 *Structural Biology* **197**, 191–198 (2017).
856 48. Zheng, S. Q. *et al.* MotionCor2: anisotropic correction of beam-induced motion for
857 improved cryo-electron microscopy. *Nat Methods* **14**, 331–332 (2017).
858 49. Mastronarde, D. N. Dual-Axis Tomography: An Approach with Alignment Methods That
859 Preserve Resolution. *Journal of Structural Biology* **120**, 343–352 (1997).
860 50. Himes, B. A. & Zhang, P. emClarity: software for high-resolution cryo-electron
861 tomography and subtomogram averaging. *Nat Methods* **15**, 955–961 (2018).
862 51. Bepler, T., Kelley, K., Noble, A. J. & Berger, B. Topaz-Denoise: general deep denoising
863 models for cryoEM and cryoET. *Nat Commun* **11**, 5208 (2020).
864 52. Castaño-Díez, D., Kudryashev, M., Arheit, M. & Stahlberg, H. Dynamo: A flexible, user-
865 friendly development tool for subtomogram averaging of cryo-EM data in high-
866 performance computing environments. *Journal of Structural Biology* **178**, 139–151
867 (2012).
868 53. Chua, E. Y. D. *et al.* 3.9 Å structure of the nucleosome core particle determined by
869 phase-plate cryo-EM. *Nucleic Acids Res* **44**, 8013–8019 (2016).
870 54. Davey, C. A., Sargent, D. F., Luger, K., Maeder, A. W. & Richmond, T. J. Solvent
871 Mediated Interactions in the Structure of the Nucleosome Core Particle at 1.9Å
872 Resolution††We dedicate this paper to the memory of Max Perutz who was particularly
873 inspirational and supportive to T.J.R. in the early stages of this study. *Journal of*
874 *Molecular Biology* **319**, 1097–1113 (2002).
875 55. Kasinath, V. *et al.* Structures of human PRC2 with its cofactors AEBP2 and JARID2.
876 *Science* **359**, 940–944 (2018).
877 56. Chen, X. *et al.* Structures of +1 nucleosome–bound PIC-Mediator complex. *Science* **378**,
878 62–68 (2022).
879 57. Horn, V. *et al.* Structural basis of specific H2A K13/K15 ubiquitination by RNF168. *Nat*
880 *Commun* **10**, 1751 (2019).

881 58. Yang, B. *et al.* Identification of cross-linked peptides from complex samples. *Nat*
882 *Methods* **9**, 904–906 (2012).
883 59. Gail, E. H., Shah, A. D., Schittenhelm, R. B. & Davidovich, C. crisscrosslinkeR:
884 identification and visualization of protein–RNA and protein–protein interactions from
885 crosslinking mass spectrometry. *Bioinformatics* **36**, 5530–5532 (2020).
886 60. Combe, C. W., Fischer, L. & Rappsilber, J. xiNET: Cross-link Network Maps With
887 Residue Resolution*. *Molecular & Cellular Proteomics* **14**, 1137–1147 (2015).
888 61. Canver, M. C. *et al.* A saturating mutagenesis CRISPR-Cas9–mediated functional
889 genomic screen identifies cis- and trans-regulatory elements of Oct4 in murine ESCs.
890 *Journal of Biological Chemistry* **295**, 15797–15809 (2020).
891 62. Seruggia, D. *et al.* TAF5L and TAF6L Maintain Self-Renewal of Embryonic Stem Cells
892 via the MYC Regulatory Network. *Molecular Cell* **74**, 1148-1163.e7 (2019).
893 63. Healy, E. *et al.* PRC2.1 and PRC2.2 Synergize to Coordinate H3K27 Trimethylation.
894 *Molecular Cell* **76**, 437-452.e6 (2019).
895 64. Martin, M. Cutadapt removes adapter sequences from high-throughput sequencing
896 reads. *EMBnet.journal* **17**, 10–12 (2011).
897 65. Langmead, B. & Salzberg, S. L. Fast gapped-read alignment with Bowtie 2. *Nat Methods*
898 **9**, 357–359 (2012).
899 66. Zhang, Y. *et al.* Model-based Analysis of ChIP-Seq (MACS). *Genome Biology* **9**, R137
900 (2008).
901 67. Amemiya, H. M., Kundaje, A. & Boyle, A. P. The ENCODE Blacklist: Identification of
902 Problematic Regions of the Genome. *Sci Rep* **9**, 9354 (2019).
903 68. Reske, J. J., Wilson, M. R. & Chandler, R. L. ATAC-seq normalization method can
904 significantly affect differential accessibility analysis and interpretation. *Epigenetics &*
905 *Chromatin* **13**, 22 (2020).
906 69. Zhu, L. J. *et al.* ChIPpeakAnno: a Bioconductor package to annotate ChIP-seq and
907 ChIP-chip data. *BMC Bioinformatics* **11**, 237 (2010).
908